

Research paper

Pinning boundary conditions for phase-field models

Hyun Geun Lee^a, Junxiang Yang^b, Junseok Kim^{b,*}^a Department of Mathematics, Kwangwoon University, Seoul 01897, Republic of Korea^b Department of Mathematics, Korea University, Seoul 02841, Republic of Korea

ARTICLE INFO

Article history:

Received 12 July 2019

Revised 9 October 2019

Accepted 15 October 2019

Available online 15 October 2019

Keywords:

Pinning boundary condition

Allen–Cahn equation

Conservative Allen–Cahn equation

ABSTRACT

In this paper, we present pinning boundary conditions for two- (2D) and three-dimensional (3D) phase-field models. For the 2D and axisymmetric domains in the neighborhood of the pinning boundaries, we apply an odd-function-type treatment and use a local gradient of the phase-field for points away from the pinning boundaries. For the 3D domain, we propose a simple treatment that fixes the values on the ghost grid points beyond the discrete computational domain. As examples of the phase-field models, we consider the Allen–Cahn and conservative Allen–Cahn equations with the pinning boundary conditions. We present various numerical experiments to demonstrate the performance of the proposed pinning boundary treatment. The computational results confirm the efficiency of the proposed method.

© 2019 Elsevier B.V. All rights reserved.

1. Introduction

We consider the Allen–Cahn (AC) and conservative Allen–Cahn (CAC) equations with the pinning boundary condition

$$\frac{\partial \phi}{\partial t} = -\frac{F'(\phi)}{\epsilon^2} + \Delta \phi, \quad (1)$$

$$\frac{\partial \phi}{\partial t} = -\frac{F'(\phi)}{\epsilon^2} + \Delta \phi + \beta(t)\sqrt{F(\phi)}, \quad (2)$$

where $\phi(\mathbf{x}, t)$ is an order parameter, $F(\phi) = 0.25(\phi^2 - 1)^2$, $\epsilon > 0$ is constant, and $\beta(t)\sqrt{F(\phi)}$ is a space-time dependent Lagrange multiplier [1]. The AC equation was originally proposed by Allen and Cahn [2] for antiphase domain coarsening. It was later applied to various fields such as image segmentation, dendritic growth, topology optimization, and motion by mean curvature [3]. By contrast, the CAC equation was applied to simulations of mass conservation systems such as multiphase flow [4,5]. For these types of equations, Neumann [6,7], Dirichlet [8,9], periodic [10], and contact angle boundary [11,12] conditions have been widely used.

However, when the phase-field method is used to simulate some specific problems such as droplet evaporation or coffee drying on a solid substrate, a particular boundary condition (i.e., pinning condition) must be considered. For the pinning effect, Peng et al. [13] proposed a theoretical model and conducted molecular dynamics simulations for the grain boundary of a moving particle. Zhou et al. [14] conducted molecular dynamics simulations to investigate the maximum pinning force.

* Corresponding author.

E-mail address: cfdkim@korea.ac.kr (J. Kim).URL: <http://math.korea.ac.kr/~cfdkim/> (J. Kim)

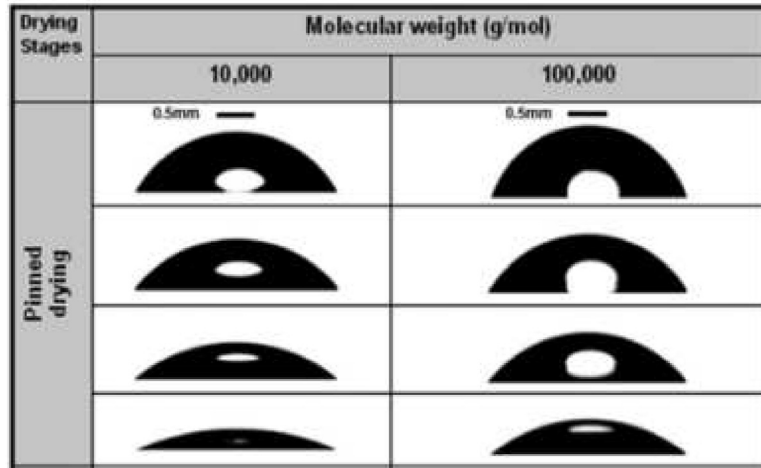


Fig. 1. Experiments of droplet drying on a solid substrate with a pinned boundary. Adapted from Mamalis et al. [16] with permission from ACS Publications.

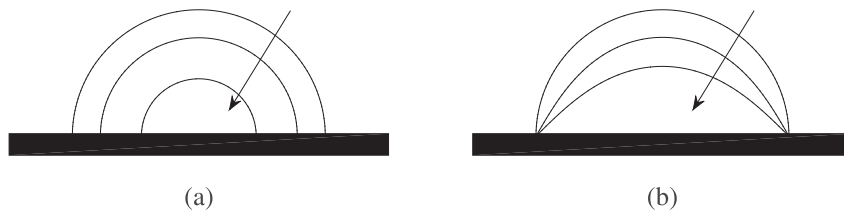


Fig. 2. (a) Constant contact angle. (b) Pinning boundary.

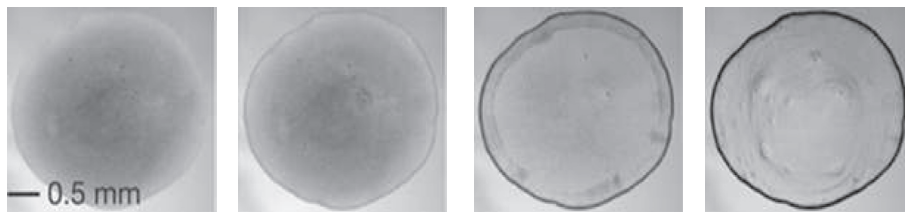


Fig. 3. Temporal evolution of experimental snapshots during evaporation of a drop of particle suspension from left to right. Adapted from Yunker et al. [18] with permission from the Nature Publishing Group.

Du et al. [15] performed numerical and analytical studies on the pinning effect on different shaped particles. To the best of our knowledge, few detailed numerical investigations of the pinning boundary condition on a flat substrate have been conducted using the phase-field method. The pinning effect on a flat substrate has been observed in many natural and scientific fields. These include droplet drying on a solid substrate with a pinned boundary [16] (see Fig. 1).

Fig. 2 (a) and (b) show a schematic illustration for the evolution processes of a droplet with constant contact angle and pinning boundary conditions, respectively, as the liquid evaporates with time.

The pinning boundary condition is one of the necessary conditions for the formation of a coffee stain [17,18], as shown in Fig. 3.

This study proposes an accurate and robust numerical method for the pinning boundary condition for two- (2D) and three-dimensional (3D) phase-field models. In particular, we focus on the AC and CAC equations as examples. In phase-field models, the Cahn-Hilliard (CH) equation is also widely used and has been studied by many researchers [19–21]; the proposed pinning boundary method can be applied to the CH equation.

The remainder of this paper is structured as follows. In Section 2, we describe the numerical solution algorithm. In Section 3, we present various numerical results to demonstrate the performance of the proposed model. A conclusion is given in Section 4.

2. Numerical solutions

We consider a 2D numerical solution and later extend it to a 3D space. We define the computational domain $\Omega = (a, b) \times (c, d)$ and grid size $h = (b - a)/N_x = (d - c)/N_y$, where N_x and N_y are integers. For $i = 1, \dots, N_x$ and $j = 1, \dots, N_y$,

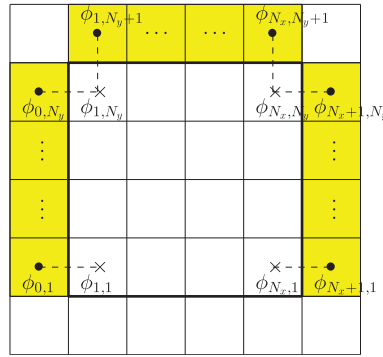


Fig. 4. Zero Neumann boundary condition for left, right, and top boundaries.

let $(x_i, y_j) = (a + (i - 0.5)h, c + (j - 0.5)h)$. Let ϕ_{ij}^n be approximations of $\phi(x_i, y_j, n\Delta t)$, where Δt is the temporal step size. An operator splitting method is adopted to solve Eq. (2):

$$\frac{\partial \phi}{\partial t} = -\frac{F'(\phi)}{\epsilon^2} + \Delta \phi, \tag{3}$$

$$\frac{\partial \phi}{\partial t} = \beta(t)\sqrt{F(\phi)}. \tag{4}$$

First, Eq. (3) is solved using an explicit scheme:

$$\frac{\phi_{ij}^* - \phi_{ij}^n}{\Delta t} = -\frac{F'(\phi_{ij}^n)}{\epsilon^2} + \Delta_h \phi_{ij}^n, \tag{5}$$

where $\Delta_h \phi_{ij}^n = (\phi_{i,j+1}^n + \phi_{i+1,j}^n + \phi_{i,j-1}^n + \phi_{i-1,j}^n - 4\phi_{ij}^n)/h^2$. Second, Eq. (4) is discretized as

$$\frac{\phi_{ij}^{n+1} - \phi_{ij}^*}{\Delta t} = \beta^* \sqrt{F(\phi_{ij}^*)}. \tag{6}$$

Using the mass conservation and Eq. (6), we get

$$\sum_{i=1}^{N_x} \sum_{j=1}^{N_y} \phi_{ij}^0 h^2 = \sum_{i=1}^{N_x} \sum_{j=1}^{N_y} \phi_{ij}^{n+1} h^2 = \sum_{i=1}^{N_x} \sum_{j=1}^{N_y} (\phi_{ij}^* + \Delta t \beta^* \sqrt{F(\phi_{ij}^*)}) h^2. \tag{7}$$

Thus,

$$\beta^* = \frac{1}{\Delta t} \frac{\sum_{i=1}^{N_x} \sum_{j=1}^{N_y} (\phi_{ij}^0 - \phi_{ij}^*)}{\sum_{i=1}^{N_x} \sum_{j=1}^{N_y} \sqrt{F(\phi_{ij}^*)}}. \tag{8}$$

Finally, we obtain ϕ^{n+1} from Eq. (6), i.e., $\phi_{ij}^{n+1} = \phi_{ij}^* + \Delta t \beta^* \sqrt{F(\phi_{ij}^*)}$. We note that Eq. (5) is a numerical solution of Eq. (1).

Next, we describe the boundary conditions. The zero Neumann boundary condition is used for ϕ on the left, right, and top boundaries of the computational domain, i.e., $\phi_x(a, y, t) = \phi_x(b, y, t) = \phi_y(x, d, t) = 0$. Fig. 4 illustrates the zero Neumann boundary condition for left, right, and top boundaries.

$$\begin{aligned} \phi_{0,j} &= \phi_{1,j} \text{ and } \phi_{N_x+1,j} = \phi_{N_x,j} \quad \text{for } 1 \leq j \leq N_y, \\ \phi_{i,N_y+1} &= \phi_{i,N_y} \quad \text{for } 1 \leq i \leq N_x. \end{aligned}$$

For the bottom boundary, we set the proposed pinning boundary condition, which is described next. For the boundary points located on the interfacial transition layer, the boundary values are obtained by $\phi_{i,0} = \tanh\left(\frac{l_1+l_2}{\sqrt{2}\epsilon}\right)$, $1 \leq i \leq N_x$, where $l_1 + l_2$ is the distance from the point (x_i, y_0) to the interface of the droplet, i.e., to the zero-level contour of ϕ ; see Fig. 5(a). Here, l_1 is the distance from point (x_i, y_1) to the interface of the droplet, i.e., $l_1 = \sqrt{2}\epsilon \tanh^{-1}(\phi_{i,1})$. We then calculate $l_2 = h \cos(\theta_1)$ and $\theta_1 = \theta_2$ from a geometry relation, that is $l_2 = h \cos(\theta_2)$, where θ_2 is an angle between the normal vector \mathbf{m} to the interface of the droplet having an initial point as point (x_i, y_1) and the y axis (see Fig. 5(b)). The x and y components of the normal vector \mathbf{m} are $m_1 = \phi_x$ and $m_2 = \phi_y$, respectively, and we approximate m_1 and m_2 using the four values $\phi_{i-1,1}$, $\phi_{i,1}$, $\phi_{i+1,1}$, and $\phi_{i,2}$ as follows: $m_1 \approx \frac{\phi_{i+1,1} - \phi_{i-1,1}}{2h}$ and $m_2 \approx \frac{\phi_{i,2} - \phi_{i,1}}{h}$. Then, the angle θ_2 is calculated as follows:

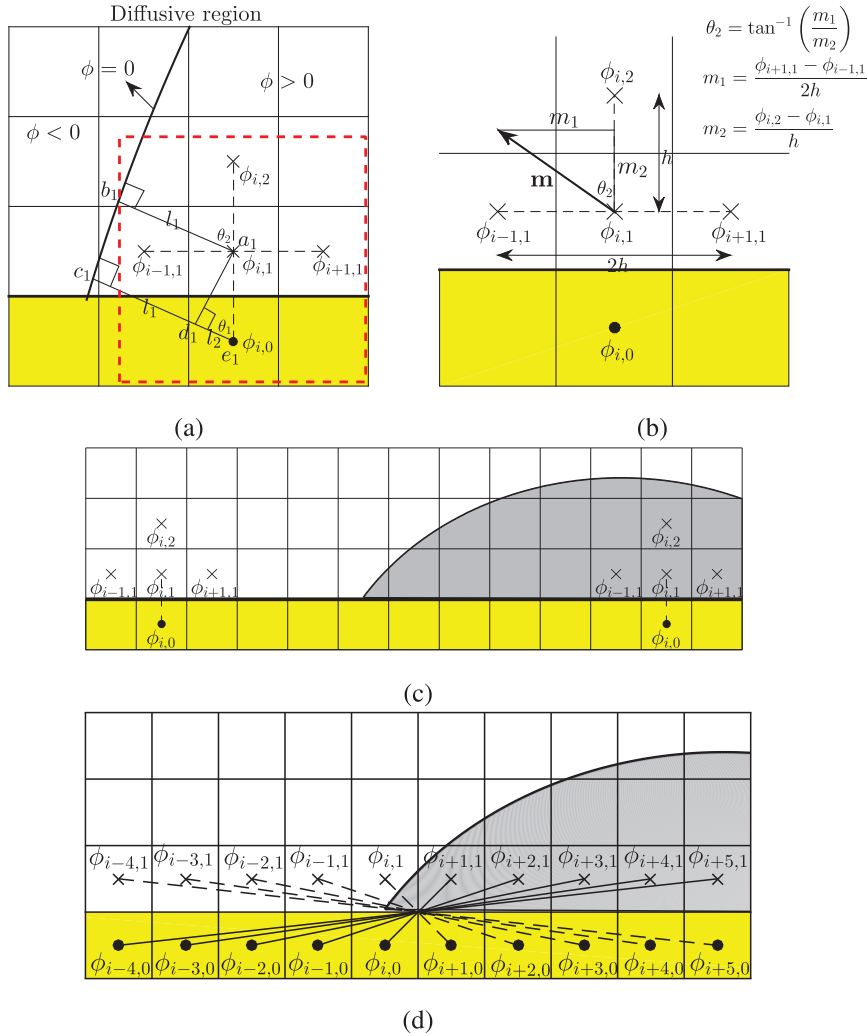


Fig. 5. Schematics of bottom boundary conditions. (a) Boundary condition for the points in the diffusive region at the left side. (b) Enlarged view of the red box region in (a). (c) Zero Neumann boundary condition for the points in the bulk phase. (d) Pinning boundary condition. (For interpretation of the references to color in this figure legend, the reader is referred to the web version of this article.)

$\theta_2 = \tan^{-1} \left(\frac{\phi_{i+1,1} - \phi_{i-1,1}}{2(\phi_{i,2} - \phi_{i,1})} \right)$. Finally, we obtain the boundary values in the diffusive region:

$$\phi_{i,0} = \tanh \left(\frac{\sqrt{2}\epsilon \tanh^{-1}(\phi_{i,1}) + h \cos \left(\tan^{-1} \left(\frac{\phi_{i+1,1} - \phi_{i-1,1}}{2(\phi_{i,2} - \phi_{i,1})} \right) \right)}{\sqrt{2}\epsilon} \right). \tag{9}$$

A schematic for the boundary values in the diffusive region located at the left of the droplet is shown in Fig. 5(a) and (b). For the diffusive region located at the right of the droplet, we calculate the boundary values in a similar manner. For the boundary points located far from the diffusive region (i.e., in the bulk phase), the zero Neumann boundary condition $\phi_{i,0} = \phi_{i,1}$ is used, which is shown in Fig. 5(c).

To achieve the pinning effect, we set the pinning boundary condition for the boundary points near the left and right endpoints located on the zero level set using the following odd function:

$$\phi(-x, -y) = \tanh \frac{\sin(\alpha)(-x) - \cos(\alpha)(-y)}{\sqrt{2}\epsilon} \tag{10}$$

$$= -\tanh \frac{\sin(\alpha)x - \cos(\alpha)y}{\sqrt{2}\epsilon} = -\phi(x, y), \tag{11}$$

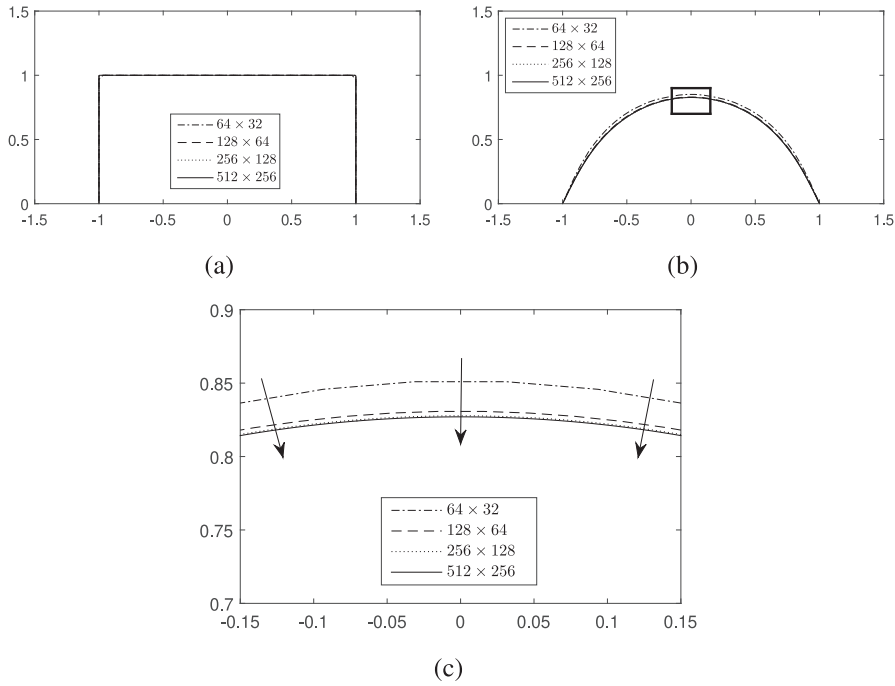


Fig. 6. Interface profiles at (a) $t = 0$ and (b) $t = 6000\Delta t$. (c) Locally enlarged view of the box region in (b). Arrows represent the convergence direction.

where α is an arbitrary angle between the interface of the droplet and a solid substrate. Thus, we set

$$\phi_{i+k-M_p,0} = -\phi_{i-k+1+M_p,1} \text{ for } k = 1, \dots, 2M_p. \quad (12)$$

Taking the left endpoint $\phi_{i,1}$ as an example, the pinning point locates in $(x_{i+1/2}, y_{1/2})$. We find M_p (integer number) positions located on the left and right sides of the pinning point, respectively. For instance, when $M_p = 5$, the pinning boundary condition (12) is

$$\begin{aligned} \phi_{i,0} &= -\phi_{i+1,1}, & \phi_{i+1,0} &= -\phi_{i,1}, \\ \phi_{i-1,0} &= -\phi_{i+2,1}, & \phi_{i+2,0} &= -\phi_{i-1,1}, \\ \phi_{i-2,0} &= -\phi_{i+3,1}, & \phi_{i+3,0} &= -\phi_{i-2,1}, \\ \phi_{i-3,0} &= -\phi_{i+4,1}, & \phi_{i+4,0} &= -\phi_{i-3,1}, \\ \phi_{i-4,0} &= -\phi_{i+5,1}, & \phi_{i+5,0} &= -\phi_{i-4,1}. \end{aligned}$$

A schematic of the pinning boundary condition is shown in Fig. 5(d).

3. Numerical experiment

3.1. Mesh convergence test

We investigate the convergence with respect to mesh size h . We use four different mesh sizes: 64×32 , 128×64 , 256×128 , and 512×256 . The other numerical parameters are: $\Delta t = 0.05/32^2$, $\epsilon = 0.06$, and $M_p = 11$. We define the following initial condition

$$\phi(x, y, 0) = \begin{cases} 1 & \text{if } -1 \leq x \leq 1, 0 \leq y \leq 1, \\ -1 & \text{otherwise} \end{cases} \quad (13)$$

on $\Omega = (-2, 2) \times (0, 2)$, which is shown in Fig. 6(a).

Fig. 6 (b) shows snapshots of the interfaces of the AC equation with different mesh sizes at $t = 6000\Delta t$. Fig. 6(c) shows the corresponding locally enlarged view in the box region shown in Fig. 6(b). As can be seen, the interface converges as the mesh size becomes increasingly finer. When mesh size 256×128 is used, we find that the interface nearly converged to the result with a finer mesh size (i.e., 512×256). Unless otherwise mentioned, we will use mesh size 256×128 in the following tests for an accurate and fast computation.

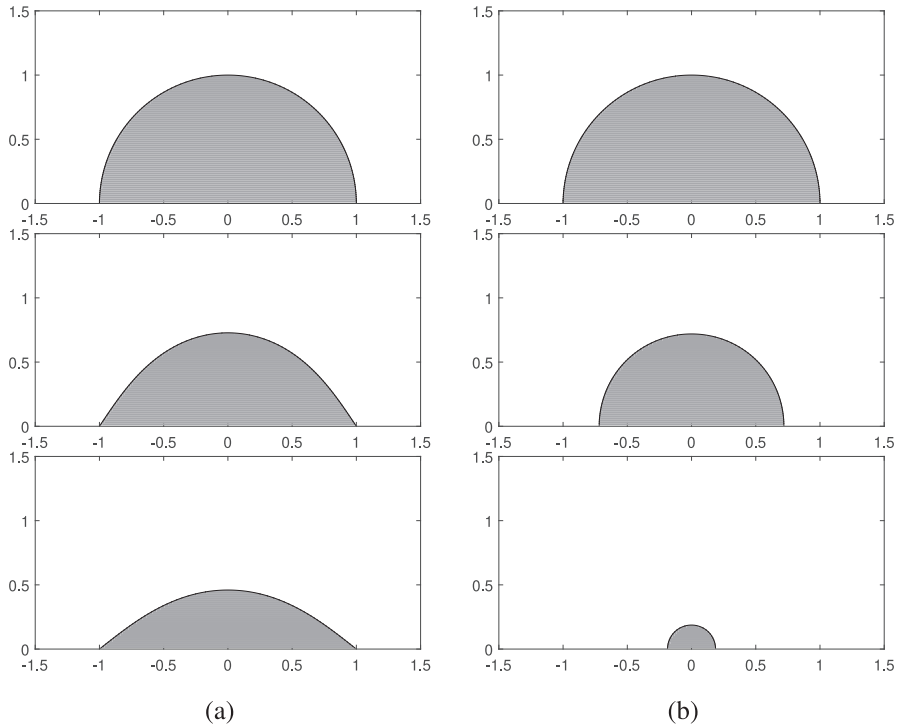


Fig. 7. Temporal evolution of the AC equation with (a) pinning boundary condition and (b) zero Neumann boundary condition. The computational times from top to bottom in each column are $t = 0, 10000\Delta t,$ and $20000\Delta t.$

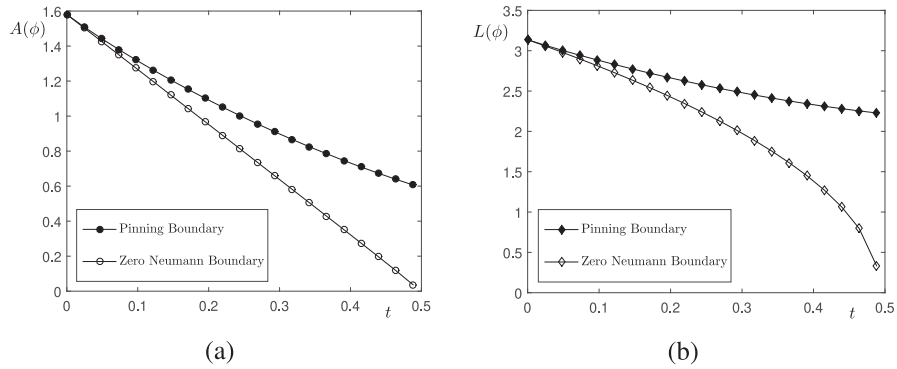


Fig. 8. Temporal evolutions of (a) total area $A(\phi)$ and (b) interfacial length $L(\phi).$

3.2. Comparison between pinning and zero Neumann boundary conditions

We focus on the effect of the pinning boundary condition on the dynamics of the AC equation. For comparison, the zero Neumann boundary condition is also considered. We use the initial condition on $\Omega = (-2, 2) \times (0, 2)$

$$\phi(x, y, 0) = \tanh\left(\frac{1 - \sqrt{x^2 + y^2}}{\sqrt{2}\epsilon}\right). \tag{14}$$

The numerical parameters are set to $h = 1/64, \Delta t = 0.1h^2, \epsilon = \epsilon_{16},$ and $M_p = 11.$ Here, $\epsilon = \epsilon_m = hm/[2\sqrt{2} \tanh^{-1}(0.9)]$ indicates that the interfacial transition layer has an approximate thickness of hm [4].

Fig. 7 (a) and (b) show the temporal evolutions of the AC equation with the same initial condition (13) for the pinning and zero Neumann boundary conditions, respectively. The total mass is defined as $M(\phi) = \int_{\Omega} 0.5(\phi(\mathbf{x}, t) + 1)d\mathbf{x}$ and the interfacial length is defined as $L(\phi) = 0.75\sqrt{2}\epsilon \int_{\Omega} |\nabla\phi(\mathbf{x}, t)|^2 d\mathbf{x}$ [22]. The temporal evolutions of total area $A(\phi)$ and interfacial length $L(\phi)$ with two different boundary conditions are shown in Fig. 8(a) and (b). Because of the effect of mean curvature

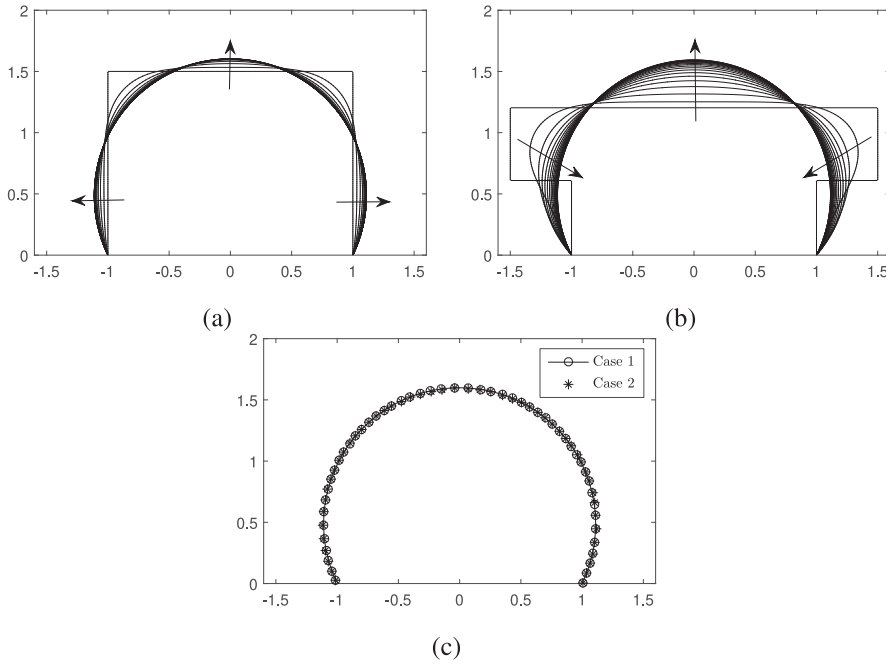


Fig. 9. Temporal evolutions of the interfacial profile for (a) case 1 and (b) case 2, where the arrows represent the evolution directions. (c) Final interfacial profiles, where the circle and star markers represent cases 1 and 2, respectively.

flow, the AC equation with zero Neumann boundary condition evolves faster. However, the dynamics of the AC equation with the pinning boundary condition are delayed.

3.3. Evolution of the CAC equation with different initial conditions

We next investigate the temporal evolution of the CAC equation with two different initial conditions. The two cases are computed using the same numerical parameters: $h = 1/64$, $\Delta t = 0.1h^2$, $\epsilon = \epsilon_{16}$, and $M_p = 11$. We stop the computation when the numerical solution reaches a numerical equilibrium state (i.e., $\|\phi^{n+1} - \phi^n\|_2 \leq 10^{-6}$). The initial conditions for cases 1 and 2 have different shapes with the same area. The initial condition for case 1 is

$$\phi_1(x, y, 0) = \begin{cases} 1 & \text{if } -1 < x < 1, y < 1.5, \\ -1 & \text{otherwise,} \end{cases} \tag{15}$$

The initial condition for case 2 is

$$\phi_2(x, y, 0) = \begin{cases} 1 & \text{if } -1 < x < 1, 0 < y < 0.61 \text{ or} \\ & -1.5 < x < 1.5, 0.61 \leq y < 1.2, \\ -1 & \text{otherwise.} \end{cases} \tag{16}$$

The temporal evolutions for the two cases are shown in Fig. 9(a) and (b), where the arrows denote the evolution directions. Fig. 9(c) shows the final interfacial profiles for the two cases. The temporal evolutions of polygonal length

$$L_p = \sum_{n=1}^{N-1} \sqrt{(X_{n+1} - X_n)^2 + (Y_{n+1} - Y_n)^2}$$

for the two cases are illustrated in Fig. 10. Here, N is the total number of points (X_n, Y_n) on the interface. We observe that those two cases evolve to nearly the same shape at the numerical equilibrium state.

3.4. Axisymmetric case

We next consider the axisymmetric AC and axisymmetric CAC equations with a pinning boundary condition of

$$\frac{\partial \phi}{\partial t} = -\frac{F'(\phi)}{\epsilon^2} + \frac{1}{r}(r\phi_r)_r + \phi_{zz}, \tag{17}$$

$$\frac{\partial \phi}{\partial t} = -\frac{F'(\phi)}{\epsilon^2} + \frac{1}{r}(r\phi_r)_r + \phi_{zz} + \beta(t)\sqrt{F(\phi)}, \tag{18}$$

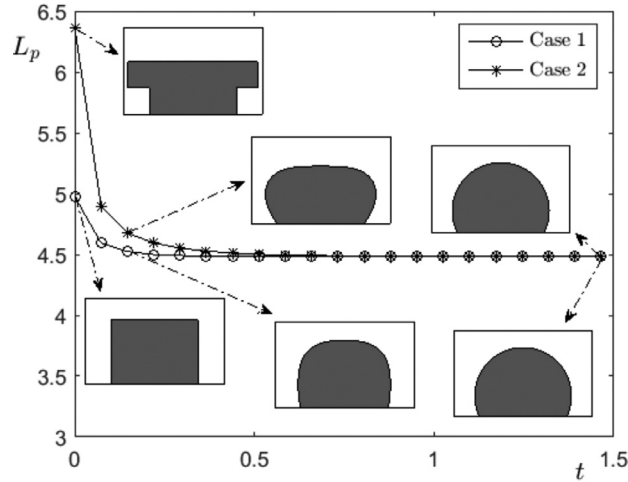


Fig. 10. Temporal evolution of polygonal length L_p for the two cases.

where $\phi(r, z, t)$ is the order parameter in the axisymmetric space. Let the computational domain be $\Omega = (0, a) \times (0, b)$. Let $\Omega_h = \{(r_i, z_k) : r_i = (i - 0.5)h, 1 \leq i \leq N_r, z_k = (k - 0.5)h, 1 \leq k \leq N_z\}$ be the discrete domain, where N_r and N_z are integers and $h = a/N_r = b/N_z$. Let ϕ_{ik}^n be the numerical approximation of $\phi(r_i, z_k, t^n)$. We describe the numerical solution for Eq. (18) because a similar manner can be used for Eq. (17). Using the operator splitting method, we can divide Eq. (18) into two parts:

$$\frac{\partial \phi}{\partial t} = -\frac{F'(\phi)}{\epsilon^2} + \frac{1}{r}(r\phi_r)_r + \phi_{zz}, \tag{19}$$

$$\frac{\partial \phi}{\partial t} = \beta(t)\sqrt{F(\phi)}. \tag{20}$$

We first solve Eq. (19) using an explicit scheme of

$$\frac{\phi_{ik}^* - \phi_{ik}^n}{\Delta t} = -\frac{F'(\phi_{ik}^n)}{\epsilon^2} + \frac{r_{i+\frac{1}{2}}(\phi_{i+1,k}^n - \phi_{ik}^n) - r_{i-\frac{1}{2}}(\phi_{ik}^n - \phi_{i-1,k}^n)}{r_i h^2} \tag{21}$$

$$+ \frac{\phi_{i,k+1}^n - 2\phi_{ik}^n + \phi_{i,k-1}^n}{h^2}, \tag{22}$$

where $r_{i+\frac{1}{2}} = 0.5(r_{i+1} + r_i)$ and $r_{i-\frac{1}{2}} = 0.5(r_i + r_{i-1})$. Second, Eq. (20) is discretized as

$$\frac{\phi_{ik}^{n+1} - \phi_{ik}^*}{\Delta t} = \beta^* \sqrt{F(\phi_{ik}^*)}. \tag{23}$$

Using the mass conservation and Eq. (23), we have

$$\sum_{i=1}^{N_r} \sum_{k=1}^{N_z} 2\pi r_i \phi_{ik}^0 h^2 = \sum_{i=1}^{N_r} \sum_{k=1}^{N_z} 2\pi r_i \phi_{ik}^{n+1} h^2 = \sum_{i=1}^{N_r} \sum_{k=1}^{N_z} 2\pi r_i (\phi_{ik}^* + \Delta t \beta^* \sqrt{F(\phi_{ik}^*)}) h^2. \tag{24}$$

Thus,

$$\beta^* = \frac{1}{\Delta t} \frac{\sum_{i=1}^{N_r} \sum_{k=1}^{N_z} r_i (\phi_{ik}^0 - \phi_{ik}^*)}{\sum_{i=1}^{N_r} \sum_{k=1}^{N_z} r_i \sqrt{F(\phi_{ik}^*)}}. \tag{25}$$

Finally, we have ϕ^{n+1} from Eq. (23), that is $\phi_{ik}^{n+1} = \phi_{ik}^* + \Delta t \beta^* \sqrt{F(\phi_{ik}^*)}$.

3.5. Effect of pinning boundary condition

To study the effect of the pinning boundary condition on the axisymmetric AC equation, we conduct a comparison study with a zero Neumann boundary condition. We define the initial condition

$$\phi(r, z, 0) = \tanh\left(\frac{1 - \sqrt{r^2 + z^2}}{\sqrt{2}\epsilon}\right) \tag{26}$$

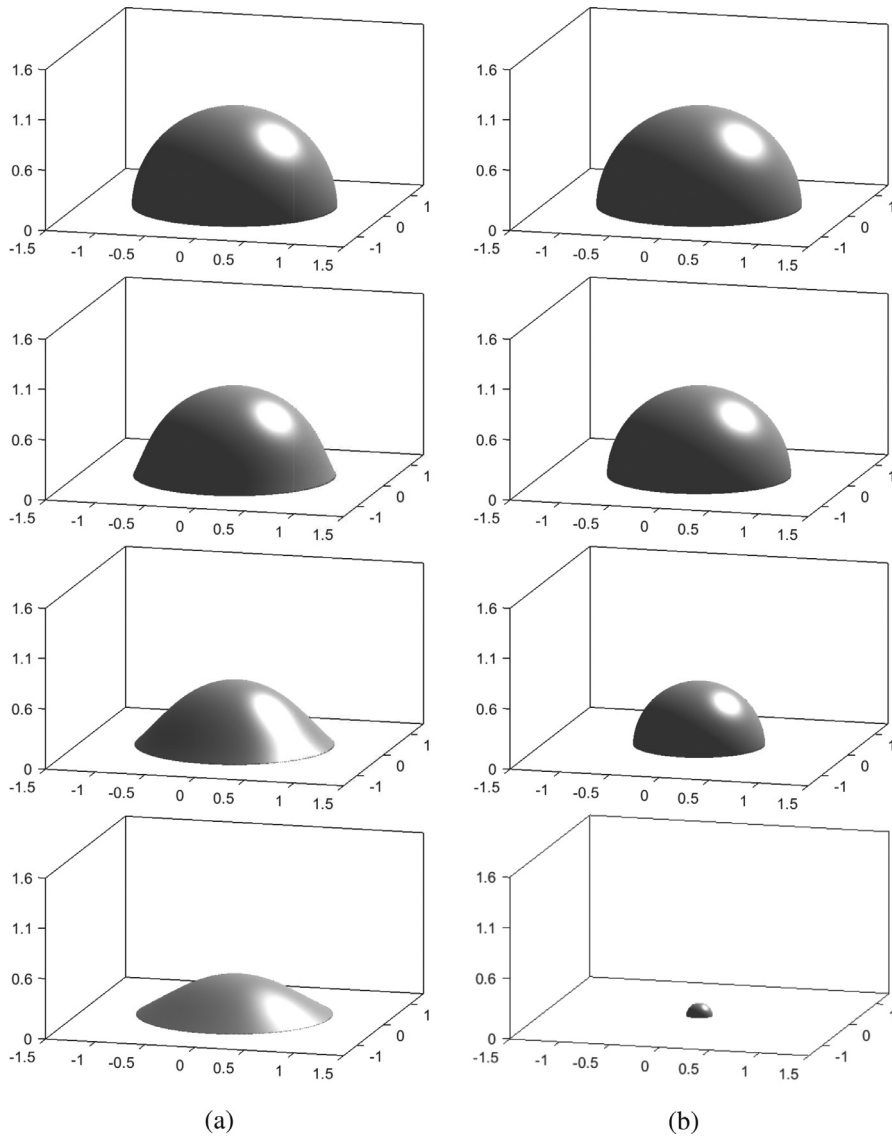


Fig. 11. Temporal evolutions of the axisymmetric AC equation with (a) pinning boundary condition and (b) zero Neumann boundary condition. The computational times from top to bottom in each column are $t = 0, 2000\Delta t, 6000\Delta t, 10000\Delta t$.

on $\Omega = (0, 2) \times (0, 2)$. The numerical parameters are taken to be the same as described in Section 3.2. The temporal evolutions of the AC equation with two different boundary conditions are shown in Fig. 11(a) and (b). The 3D views are obtained by an interpolation from $r - z$ domain. We define the discrete total volume $V(\phi)$ and surface area S as:

$$V(\phi) = h^2 \sum_{i=1}^{N_r} \sum_{k=1}^{N_z} \pi r_i (\phi_{ik} + 1), \tag{27}$$

$$S = \sum_{n=1}^{N-1} 2\pi R_{n+\frac{1}{2}} \sqrt{(R_{n+1} - R_n)^2 + (Z_{n+1} - Z_n)^2}, \tag{28}$$

where N is the total number of points on the interface, $R_{n+\frac{1}{2}} = 0.5(R_{n+1} + R_n)$, and R_n and Z_n represent the r and z coordinates of the n th point, respectively. The temporal evolutions of discrete total volume $V(\phi)$ and surface area S are shown in Fig. 12(a) and (b), respectively. As it can be seen, the dynamics of the axisymmetric AC equation are delayed with the pinning boundary condition.

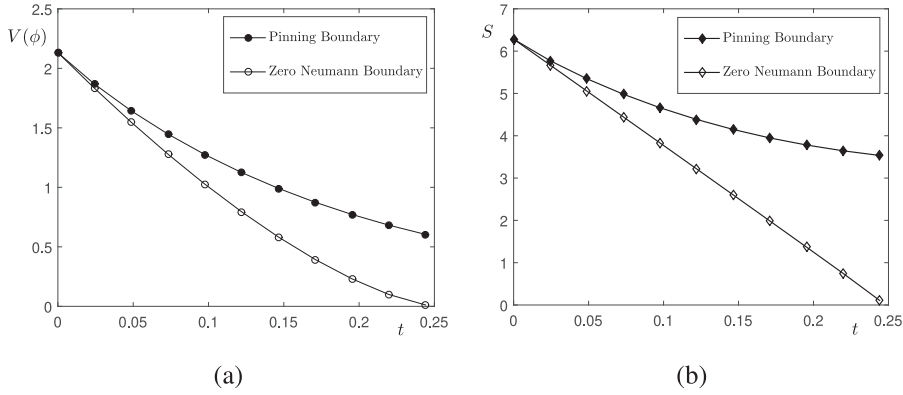


Fig. 12. Temporal evolutions of (a) total volume $V(\phi)$ and (b) surface area S .

3.6. Temporal evolution of the CAC equation with pinning boundary condition

We investigate the temporal evolution of the CAC equation with a pinning boundary condition. We use two initial conditions with different shapes and the same volume. Case 1 is

$$\phi_1(r, z, 0) = \begin{cases} 1 & \text{if } r < 1, z < 1, \\ -1 & \text{otherwise.} \end{cases} \tag{29}$$

The case 2 is

$$\phi_2(r, z, 0) = \begin{cases} 1 & \text{if } r < 0.6, z < 1.35 \text{ or } 0.6 \leq r < 1, z < 0.8, \\ -1 & \text{otherwise.} \end{cases} \tag{30}$$

The simulation is performed on an axisymmetric domain $\Omega = (0, 2) \times (0, 2)$. Here, we use $h = 1/32$, $\Delta t = 0.1h^2$, $\epsilon = 0.03$, and $M_p = 11$. The computation stops when the numerical equilibrium state is reached. Fig. 13 illustrates the temporal evolutions of the CAC equation with two cases 1 and 2. The evolutions of surface area S for the two cases are shown in Fig. 14(a). Fig. 14(b) shows the final interfacial profiles, where the star and circle markers represent the results for cases 1 and 2, respectively. We find that those two cases evolve to nearly the same final result.

3.7. Pinning boundary condition in 3D space

The previous sections described how we investigated the pinning boundary condition for 2D and axisymmetric cases. Although the proposed method works well for both cases, applying it to the fully 3D space is quite difficult and complex. In this section, we present a new simple and robust treatment of the pinning boundary condition in 3D space and that can be used for nonaxisymmetric objects. We first briefly introduce the numerical solution for the governing equation in a 3D discrete domain. We define the computational domain $\Omega = (a, b) \times (c, d) \times (e, f)$ and grid size $h = (b - a)/N_x = (d - c)/N_y = (f - e)/N_z$, where N_x, N_y , and N_z are integers. For $i = 1, \dots, N_x$, $j = 1, \dots, N_y$, and $k = 1, \dots, N_z$, let $(x_i, y_j, z_k) = (a + (i - 0.5)h, c + (j - 0.5)h, e + (k - 0.5)h)$. Let ϕ_{ijk}^n be approximations of $\phi(x_i, y_j, z_k, n\Delta t)$. First, Eq. (1) is solved using an explicit scheme:

$$\frac{\phi_{ijk}^* - \phi_{ijk}^n}{\Delta t} = -\frac{F'(\phi_{ijk}^n)}{\epsilon^2} + \Delta_h \phi_{ijk}^n, \tag{31}$$

where $\Delta_h \phi_{ijk}^n = (\phi_{i-1,j,k}^n + \phi_{i,j-1,k}^n + \phi_{i,j,k-1}^n + \phi_{i+1,j,k}^n + \phi_{i,j+1,k}^n + \phi_{i,j,k+1}^n - 6\phi_{ijk}^n)/h^2$. Second, Eq. (2) is discretized as

$$\frac{\phi_{ij,k}^{n+1} - \phi_{ij,k}^*}{\Delta t} = \beta^* \sqrt{F(\phi_{ij,k}^*)}. \tag{32}$$

Using the mass conservation and Eq. (32), we get

$$\begin{aligned} \sum_{i=1}^{N_x} \sum_{j=1}^{N_y} \sum_{k=1}^{N_z} \phi_{ijk}^0 h^3 &= \sum_{i=1}^{N_x} \sum_{j=1}^{N_y} \sum_{k=1}^{N_z} \phi_{ijk}^{n+1} h^3 \\ &= \sum_{i=1}^{N_x} \sum_{j=1}^{N_y} \sum_{k=1}^{N_z} \left(\phi_{ijk}^* + \Delta t \beta^* \sqrt{F(\phi_{ijk}^*)} \right) h^3. \end{aligned}$$

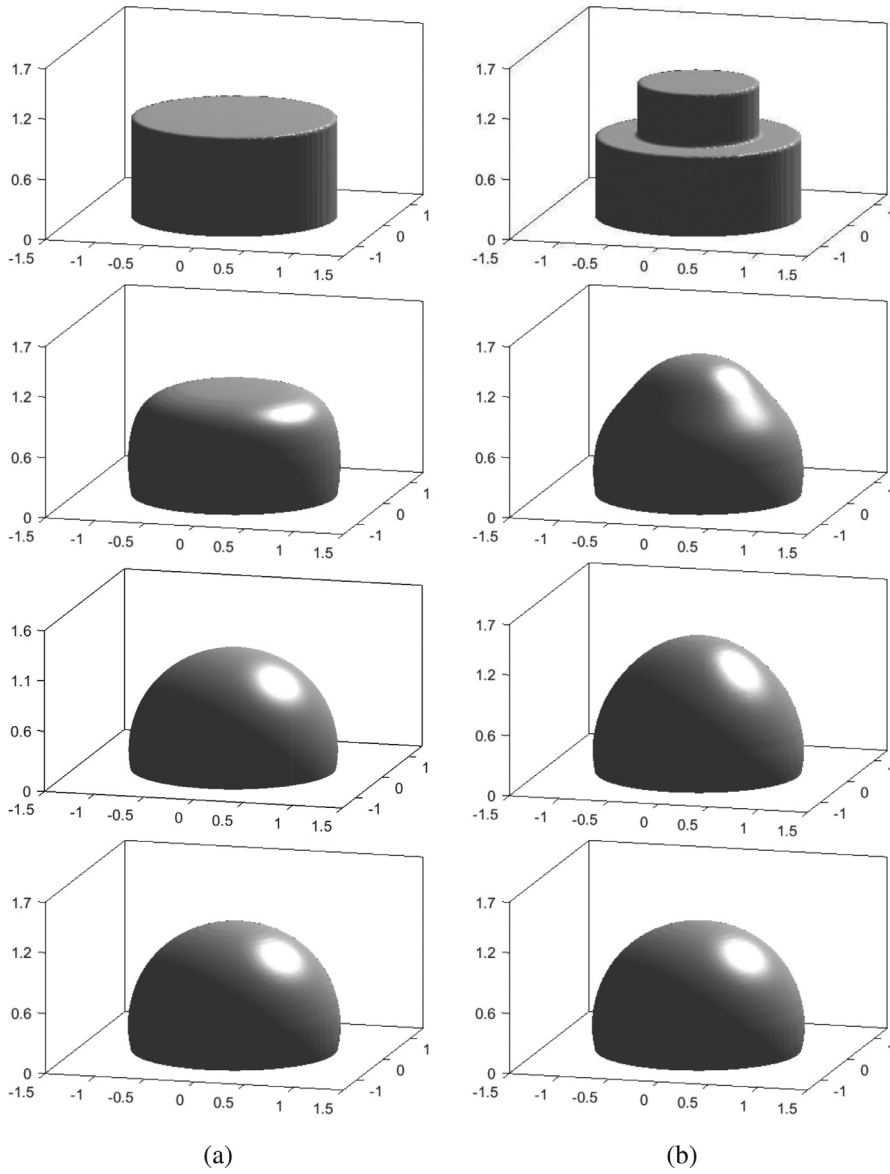


Fig. 13. Temporal evolutions of the axisymmetric CAC equation with two different initial conditions. (a) Case 1. (b) Case 2. The computational times from top to bottom in each column are $t = 0, 1000\Delta t, 1500\Delta t, 8000\Delta t$.

Thus,

$$\beta^* = \frac{1}{\Delta t} \sum_{i=1}^{N_x} \sum_{j=1}^{N_y} \sum_{k=1}^{N_z} (\phi_{ijk}^0 - \phi_{ijk}^*) / \sum_{i=1}^{N_x} \sum_{j=1}^{N_y} \sum_{k=1}^{N_z} \sqrt{F(\phi_{ijk}^*)}. \tag{33}$$

Finally, we obtain ϕ^{n+1} from Eq. (32), i.e., $\phi_{ijk}^{n+1} = \phi_{ijk}^* + \Delta t \beta^* \sqrt{F(\phi_{ijk}^*)}$. Next, we describe the boundary conditions. The zero Neumann boundary condition is used for all boundaries except the bottom, i.e., $\phi_x(a, y, z, t) = \phi_x(b, y, z, t) = \phi_y(x, c, z, t) = \phi_y(x, d, z, t) = \phi_z(x, y, f, t) = 0$.

$$\begin{aligned} \phi_{0jk} &= \phi_{1jk}, & \phi_{N_x+1,jk} &= \phi_{N_x,jk} & \text{for } 1 \leq j \leq N_y, 1 \leq k \leq N_z, \\ \phi_{i0k} &= \phi_{i1k}, & \phi_{i,N_y+1,k} &= \phi_{i,N_y,k} & \text{for } 1 \leq i \leq N_x, 1 \leq k \leq N_z, \\ \phi_{ij,N_z+1} &= \phi_{ij,N_z} & \text{for } 1 \leq i \leq N_x, 1 \leq j \leq N_y. \end{aligned}$$

For the bottom boundary, we set the proposed pinning boundary condition, which is defined as

$$\phi_{ij0}^n = \phi_{ij0}^p \quad \text{for } 1 \leq i \leq N_x, 1 \leq j \leq N_y, n \geq p,$$

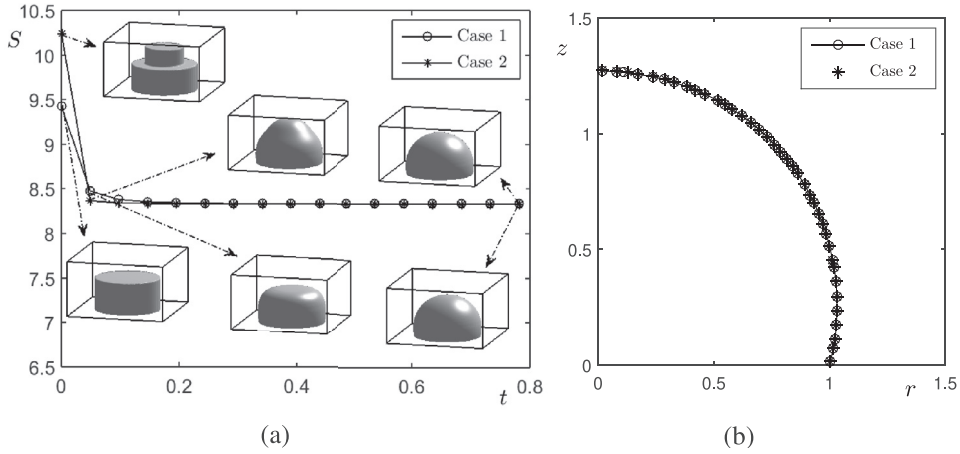


Fig. 14. (a) Temporal evolutions of surface area S with cases 1 and 2. (b) Equilibrium interfacial profiles for case 1 (star markers) and case 2 (circle markers).

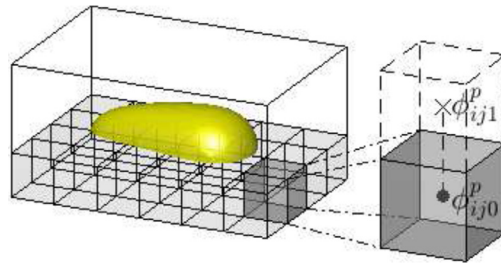


Fig. 15. Schematic of the pinning boundary condition in 3D space.

where $\phi_{ij0}^p = \phi_{ij1}^p$ for the some starting pinning time $t = p\Delta t$. A schematic is shown in Fig. 15. The pinning effect starts from a specific time $t = p\Delta t$ and lasts until the final time.

To show the efficiency of the proposed pinning boundary condition for nonaxisymmetric 3D objects (e.g., Fig. 16(a)), we numerically investigate the evolution of nonaxisymmetric initial conditions using the following parameters: $\Omega = (0, 2) \times (0, 2) \times (0, 1)$, $h = 1/128$, $\Delta t = 0.1h^2$, and $\epsilon = \epsilon_4$. The pinning effect starts at $t = 2000\Delta t$. We consider a “Y”-shaped initial condition as shown in Fig. 16(b). Fig. 16(c) shows the temporal evolutions of the scaled total volume $\bar{V}(\phi^n) = V(\phi^n)/V(\phi^0)$ for the AC and CAC equations, where $V(\phi^n) = \sum_{i=1}^{N_x} \sum_{j=1}^{N_y} \sum_{k=1}^{N_z} 0.5(\phi_{ijk}^n + 1)h^3$. We note that the nonaxisymmetric pinning phenomenon, such as the nonaxisymmetric stain formation [23] as shown in Fig. 16(a), occurs in many natural and engineering fields.

3.8. Effect of M_p number on the efficiency and accuracy

Here, we investigate the effect of the M_p number on the efficiency and accuracy of the proposed pinning boundary condition. For the AC equation, the computational domain is set to $\Omega = (-2, 2) \times (0, 2)$ with mesh size $h = 1/64$. In the simulation, we use $\Delta t = 0.1h^2$, $\epsilon = 0.06$, and different M_p numbers: $M_p = 5, 6, \dots, 11$. The initial condition is:

$$\phi(x, y, 0) = \begin{cases} 1 & \text{if } -1.5 < x < 1.5, y < 0.3, \\ -1 & \text{otherwise.} \end{cases} \quad (34)$$

For the CAC equation, we use various M_p numbers $M_p = 1, 2, \dots, 5$. The other numerical parameters are the same as before. The initial condition on the domain $\Omega = (-1, 1) \times (0, 4)$ is:

$$\phi(x, y, 0) = \begin{cases} 1 & \text{if } -0.2 < x < 0.2, y < 1.8, \\ -1 & \text{otherwise.} \end{cases} \quad (35)$$

Figs. 17(a) and 18(a) illustrate the initial conditions for the AC and CAC equations, respectively. Fig. 17(b)–(d) show snapshots of the filled contours at the zero level of the numerical solutions of the AC equation at $t = 85000\Delta t$ with different M_p numbers $M_p = 5, 8$, and 11, respectively. We find that the pinning condition does not work well with $M_p = 5$. Fig. 18(b) and (c) show snapshots for the case of the CAC equation at an equilibrium state (i.e., $\|\phi^{n+1} - \phi^n\|_2 \leq 10^{-6}$) with $M_p = 1$

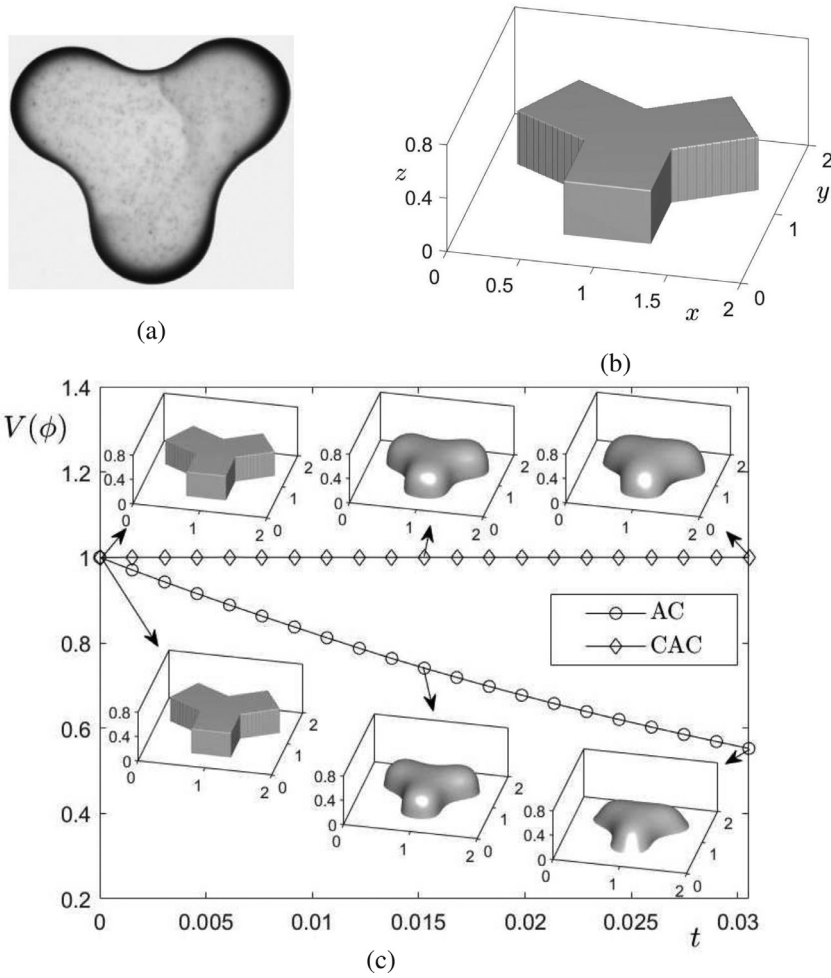


Fig. 16. (a) Nonaxisymmetric stain. Adapted from Deegan et al. [23] with permission from the Nature Publishing Group. (b) Initial condition. (c) Temporal evolutions of total volume for AC and CAC, where the small figures are the evolutions at the corresponding time steps.

and 5, respectively. We find that the pinning condition does not work well with $M_p = 1$ in the case of the CAC equation. In general, the CAC equation requires fewer M_p numbers to achieve the pinning condition as compared to the AC equation in 2D space. The CPU times for the AC and CAC equations with respect to different M_p numbers are shown in Fig. 19(a) and (b), respectively. From the results shown in Figs. 17–19, we observe that an increase in the number of M_p improved the accuracy and reduced the efficiency of the scheme.

3.9. Comparison of the results in 2D and 3D spaces

Finally, we compare the different dynamics of the AC and CAC equations in 2D and 3D spaces. For 3D space, the cube with length L_x , width L_y , height L_z , and center $(0,0,0.5)$ is chosen as the initial shape. The values of ϕ are set to 1 inside and -1 outside the cube. For 2D space, we consider its corresponding 3D shape with an imaginary width L_y , which is shown in Fig. 20, where L_y is the imaginary width and s represents the arc length. In this simulation, the computational domains are $\Omega = (-1, 1) \times (-1, 1) \times (0, 2)$ and $\Omega = (-1, 1) \times (0, 2)$ for the 2D and 3D cases, respectively. The other parameters are $h = 1/64$, $\Delta t = 0.1h^2$, and $\epsilon = \epsilon_4$. Fig. 21(a) and (b) show the temporal evolutions of the AC equation in 2D and 3D spaces, respectively. The temporal evolutions of total volume $V(\phi)$ and surface area S are illustrated in Fig. 22(a) and (b). We can observe that the evolutions of the AC equation in 3D space are faster than those in 2D space because of the stronger effect of curvature in 3D space. Fig. 23(a) and (b) show the temporal evolutions of the CAC equation in 2D and 3D spaces, respectively. Note that because the total volume is constant for the CAC equation, we show only the temporal evolutions of surface area for the CAC equation in Fig. 24.

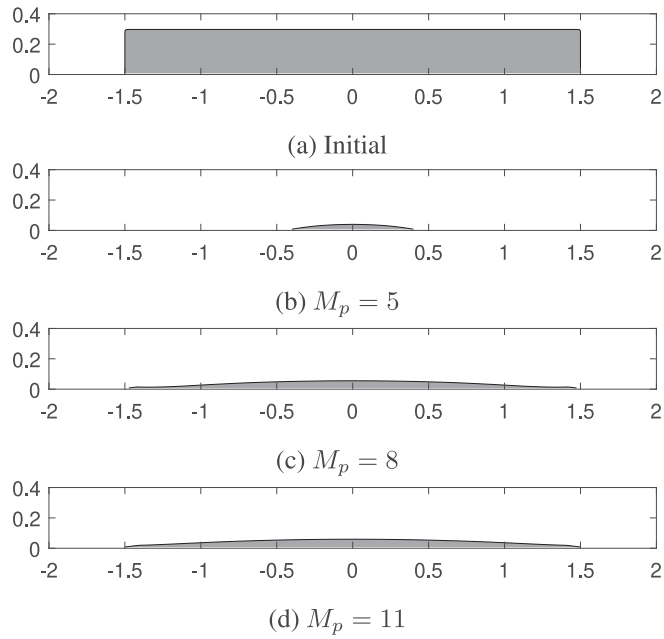


Fig. 17. Snapshots of the numerical solutions from the AC equation with respect to different M_p numbers: (b) $M_p = 5$, (c) $M_p = 8$, and (d) $M_p = 11$ at $t = 85000\Delta t$.

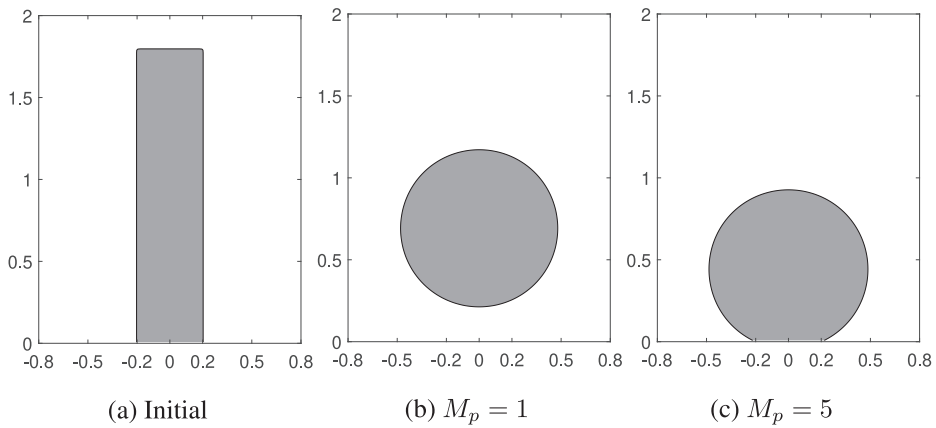


Fig. 18. Snapshots of the numerical solutions from the CAC equation with respect to different M_p numbers: (b) $M_p = 1$ and (c) $M_p = 5$ at equilibrium state.

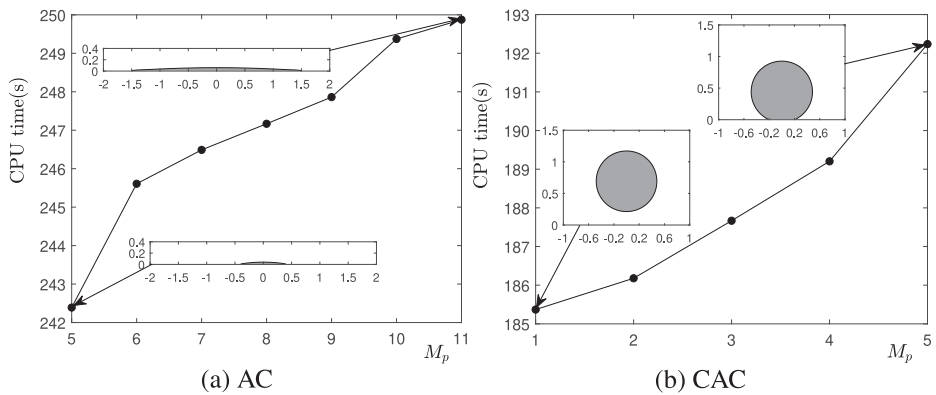


Fig. 19. CPU times with respect to different M_p numbers for the (a) AC and (b) CAC equations. The embedded figures represent the snapshots at specific time steps.

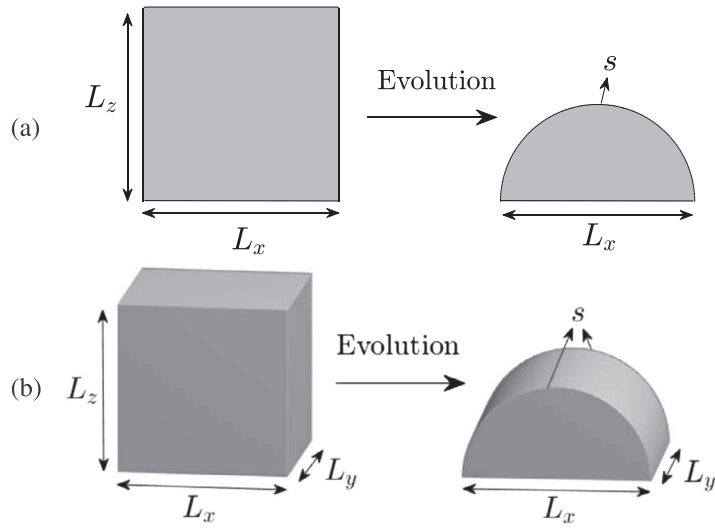


Fig. 20. Schematic illustrations of the evolution in (a) 2D and its (b) 3D image.

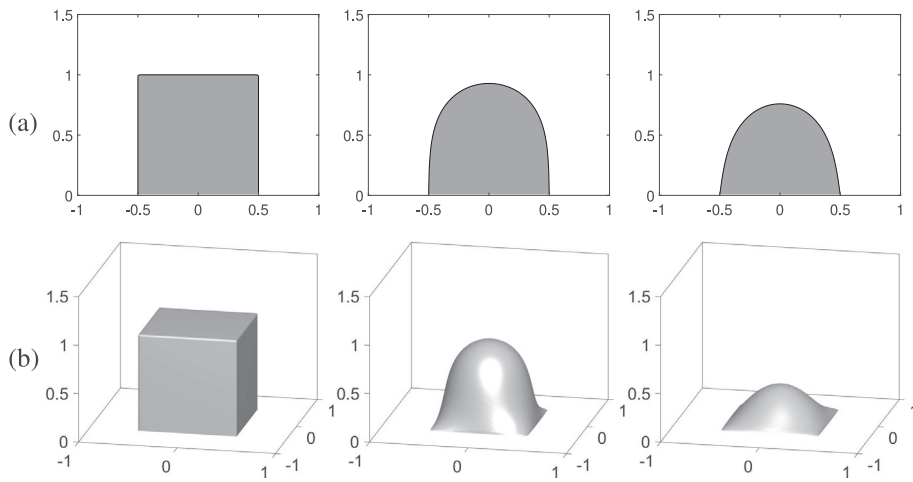


Fig. 21. Temporal evolutions of the AC equation in (a) 2D and (b) 3D spaces. Computational times from left to right in each row are $\Delta t = 0, 2750\Delta t, \text{ and } 5500\Delta t$.

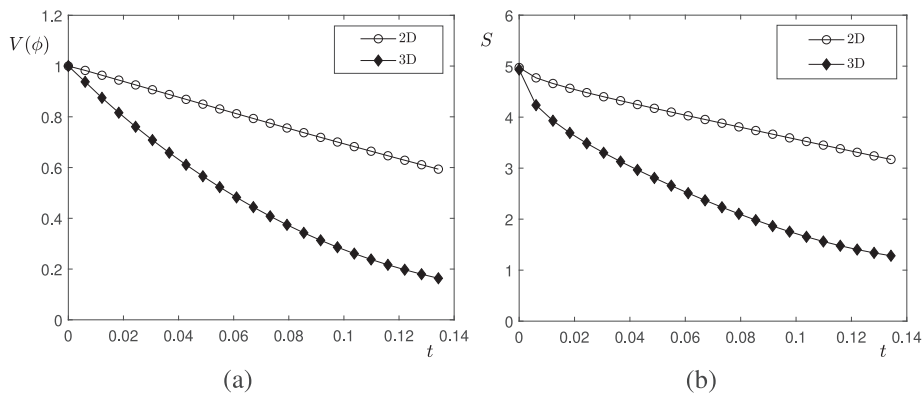


Fig. 22. Temporal evolutions of (a) total volume and (b) surface area of the AC equation in 2D and 3D spaces.

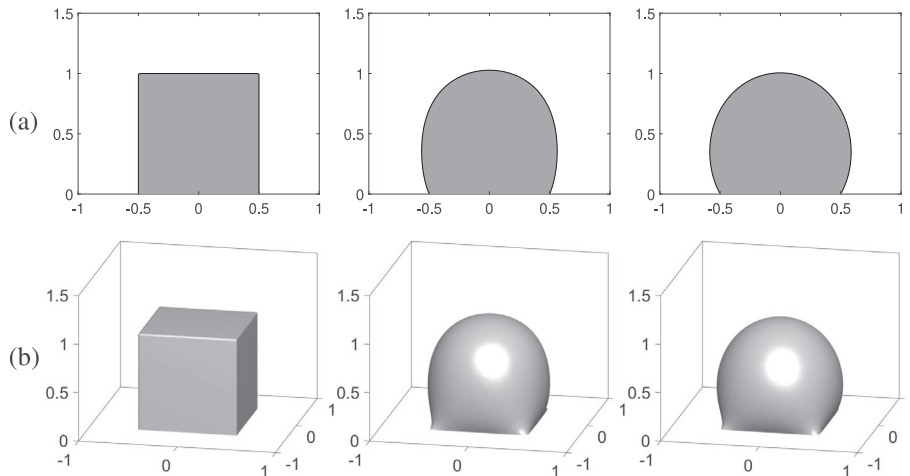


Fig. 23. Temporal evolutions of the CAC equation in (a) 2D and (b) 3D spaces. Computational times from left to right are $\Delta t = 0$, $2750\Delta t$, and $5500\Delta t$.

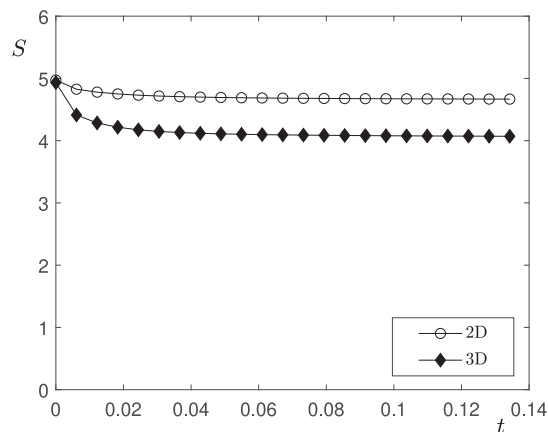


Fig. 24. Temporal evolutions of surface area of the CAC equation in 2D and 3D spaces.

4. Conclusion

In this study, we proposed pinning boundary conditions for 2D and 3D phase-field models. For the 2D and axisymmetric domains, in the neighborhood of the pinning boundaries, we applied an odd-function-type treatment and used a local gradient of the phase-field for points away from the pinning boundaries. For the 3D domain, we proposed a very simple scheme that fixes the values at the ghost grid points beyond the discrete computational domain. We presented various numerical experiments to demonstrate the performance of the proposed pinning boundary treatment for the AC and CAC equations. The computational results confirmed the good performance of the proposed method. Future research will include evaporation of liquid drops on a substrate to enable us to model the coffee-ring effect.

Declaration of Competing Interest

We declare that we have no financial and personal relationships with other people or organizations that can inappropriately influence our work, there is no professional or other personal interest of any nature or kind in any product, service and/or company that could be construed as influencing the position presented in, or the review of, the manuscript entitled, Pinning boundary condition for phase-field models.

Acknowledgments

The first author (H.G. Lee) was supported by the Research Grant of Kwangwoon University in 2020 and by Basic Science Research Program through the National Research Foundation of Korea (NRF) funded by the Ministry of Education (NRF-2019R1C1C1011112). The corresponding author (J.S. Kim) was supported by Basic Science Research Program through the National Research Foundation of Korea (NRF) funded by the Ministry of Education (NRF-2019R1A2C1003053).

References

- [1] Brassel M, Bretin E. A modified phase field approximation for mean curvature flow with conservation of the volume. *Math Method Appl Sci* 2011;34:1157–80.
- [2] Allen SM, Cahn JW. A microscopic theory for antiphase boundary motion and its application to antiphase domain coarsening. *Acta Mater* 1979;27:1085–95.
- [3] Bretin E, Danescu A, Penuelas J, Masnou S. Multiphase mean curvature flows with high mobility contrasts: a phase-field approach, with applications to nanowires. *J Comput Phys* 2018;365:324–49.
- [4] Jeong D, Kim J. Conservative Allen–Cahn–Navier–Stokes system for incompressible two-phase fluid flows. *Comput Fluids* 2017;156(12):239–46.
- [5] Aihara S, Takaki T, Takada N. Multi-phase-field modeling using a conservative Allen–Cahn equation for multiphase flow. *Comput Fluids* 2019;178(15):141–51.
- [6] Jeong D, Kim J. An explicit hybrid finite difference scheme for the Allen–Cahn equation. *J Comput Appl Math* 2018;340:247–55.
- [7] Lee HG. High-order and mass conservative methods for the conservative Allen–Cahn equation. *Comput Math Appl* 2016;72:620–31.
- [8] Li C, Huang Y, Yi N. An unconditionally energy stable second order finite element method for solving the Allen–Cahn equation. *J Comput Appl Math* 2019;353:38–48.
- [9] Song H, Jiang L, Li Q. A reduced order method for Allen–Cahn equations. *J Comput Appl Math* 2016;292:213–29.
- [10] Shen J, Xu J, Yang J. The scalar auxiliary variables (SAV) approach for gradient flows. *J Comput Phys* 2018;353:407–16.
- [11] Lee HG, Kim J. Accurate contact angle boundary conditions for the Cahn–Hilliard equations. *Comput Fluids* 2011;44:178–86.
- [12] Dong S. On imposing dynamic contact-angle boundary conditions for wall-bounded liquid-gas flows. *Comput Methods Appl Mech Eng* 2012;247–248:179–200.
- [13] Peng HR, Liu W, Hou HY, Liu F. Pinning effect of coherent particles on moving planar grain boundary: theoretical models and molecular dynamics simulations. *Materialia* 2019;5:100225.
- [14] Zhou J, Li W, Zhao B, Ren F. Direct measurement of the maximum pinning force during particle-grain boundary interaction via molecular dynamics simulations. *Acta Mater* 2018;148(15):1–8.
- [15] Du L, Yang S, Zhang P, Du H. Pinning effect of different shape second-phase particles on grain growth in polycrystalline: numerical and analytical investigations. *Compos Interface* 2018;25(4):357–68.
- [16] Mamalis D, Koutsos V, Sefiane K, Kagkoura A, Kalloudis M, Shanahan MER. Effect of poly(ethylene oxide) molecular weight on the pinning and pillar formation of evaporating sessile droplets: The role of the interface. *Langmuir* 2015;31(21):5908–18.
- [17] Tarafdar S, Tarasevich YY, Choudhury MD, Dutta T, Zang D. Droplet drying patterns on solid substrates: from hydrophilic to superhydrophobic contact to levitating drops. *Adv Cond Matter Phys* 2018;2018:5214924.
- [18] Yunker PJ, Still T, Lohr MA, Yodh AG. Suppression of the coffee-ring effect by shape-dependent capillary interactions. *Nature* 2011;476: 308–811.
- [19] Zhao J, Chen L, Wang H. On power law scaling dynamics for time-fractional phase field models during coarsening. *Commun Nonlinear Sci Numer Simul* 2019;70:257–70.
- [20] Jeong D, Yang J, Kim J. A practical and efficient numerical method for the Cahn–Hilliard equation in complex domains. *Commun Nonlinear Sci Numer Simul* 2019;73(15):217–28.
- [21] Jeong D, Choi Y, Kim J. A benchmark problem for the two- and three-dimensional Cahn–Hilliard equations. *Commun Nonlinear Sci Numer Simul* 2018;61:149–59.
- [22] Shin J, Jeong D, Li Y, Choi Y, Kim J. A hybrid numerical method for the phase-field model of fluid vesicles in three-dimensional space. *Int J Numer Meth Fluids* 2015;78:63–75.
- [23] Deegan RD, Bakajin O, Dupont TF, Huber G, Nagel SR, Witten TA. Capillary flow as the cause of ring stains from dried liquid drops. *Nature* 1997;389:827–9.